Journal of Catalysis 330 (2015) 354–361

Contents lists available at ScienceDirect

Journal of Catalysis

journal homepage: www.elsevier.com/locate/jcat

Sonogashira cross-coupling on the Au(111) and Au(100) facets of gold nanorod catalysts: Experimental and computational investigation

Jizhi Lin [a,b,1], Hadi Abroshan [c,1], Chao Liu [a], Manzhou Zhu [b], Gao Li [a,*], Masatake Haruta [a]

[a] State Key Laboratory of Catalysis and Gold Catalysis Researcher Centre, Dalian Institute of Chemical Physics, Chinese Academy of Sciences, Dalian 116023, China
[b] College of Chemistry and Chemical Engineering, Anhui University, Hefei 230601, China
[c] Department of Chemistry, Carnegie Mellon University, Pittsburgh, PA 15213, United States

ARTICLE INFO

Article history:
Received 28 May 2015
Revised 17 July 2015
Accepted 18 July 2015

Keywords:
Au nanorods
DFT calculation
Sonogashira cross-coupling
Au(111)
Au(100)

ABSTRACT

The catalytic activity of well-defined gold nanorods enclosed by Au(111) and Au(100) surfaces is investigated for the Sonogashira cross-coupling reaction between phenylacetylene and 4-iodoanisole, which gives rise to two homo-coupling products (diphenyldiacetylene, PhC≡C—C≡CPh and 4,4′-dimethoxy-1,1′-biphenyl, $MeOC_6H_4$—C_6H_4OMe) and a cross-coupling product (1-methoxy-4-(2-phenylethynyl)benzene, PhC≡CC_6H_4OMe). This study shows that shorter nanorods (~33 nm) with a higher percentage of Au(111) surface are considerably more selective toward the cross-coupling product (57% conversion with 90% selectivity). The selectivity of longer nanorods (e.g., 42 and 50 nm) with a higher percentage of Au(100) surface, as well as of corresponding shapeless gold nanoparticles (e.g., 2–4 and 20 nm), is found to be less than 59%. The catalytic mechanism of the homo- and cross-coupling reactions, in particular, roles played by Au(100) and Au(111) surfaces, is examined via DFT simulation. It is found that iodobenzene adsorption, C—I bond dissociation, reactant surface diffusion, and coupling reactions are more favorable on Au(111) than on Au(100). This work demonstrates the gold facet effect on catalytic coupling reactions, and the combined approach of experiment and theory permits mechanistic understanding at the molecular level.

1. Introduction

Carbon—carbon coupling reactions, including Sonogashira cross-coupling, have a central place in the evolution of organic chemistry and in grasping its essence. This type of reaction plays a large role in new carbon—carbon bond-forming [1–4]. Traditionally, palladium (Pd) complexes are the catalysts for carbon—carbon coupling reactions via homogeneous processes [5]. Unfortunately, these homogeneous catalysts suffer from some drawbacks, such as poor reusability and difficulty in removing catalysts from the products. In the search for alternatives, heterogeneous catalysts have been developed in the form of metal nanoparticles (Pd, Au, etc.) [6–9].

Over the past few decades, colloidal gold nanoparticles (NPs) have gained tremendous attention as catalysts for organic reactions such as selective oxidation, hydrogenation, and carbon—carbon coupling reactions due to the robust and green nature of gold catalysts [10–16]. According to a previous work by Lambert et al., oxide-supported gold nanoparticles are active catalysts for Sonogashira cross-coupling reactions between iodobenzene (IB) and phenylacetylene (PA) [17]. The importance of the particle size was examined, and it is found that large gold particles (23 nm) showed much more catalytic activity and selectivity than small ones (12 and 2.8 nm). This finding indicates that catalyzed Sonogashira cross-coupling is a predominantly heterogeneous process, in which the catalytically active species are associated with the metallic gold surfaces [17]. Unfortunately, the gold nanoparticles used in the experiments were shapeless and surface-undefined, which made it difficult to establish definitive structure–activity relationships and to pursue the fundamental mechanistic understanding of heterogeneous catalysis.

In the Sonogashira cross-coupling reaction between IB and PA, homo-coupling of the reactant molecules may also occur on the gold surface to yield two homo-coupling products: biphenyl (BP) and diphenyldiacetylene (DPDA). The two competitive reactions (i.e., Glaser and Ullmann homo-coupling, Scheme 1) decrease the final selectivity of the catalysts toward the desired cross-coupling product, which is diphenylacetylene (DPA). A previous study by Kanuru et al. indicated that the catalytic reaction between aryl halides and alkynes over an extended Au(111) surface yielded by 20% and 40% of cross-coupling and homo-coupling products, respectively [18]. Recent density functional theory (DFT) studies

* Corresponding author.
E-mail address: gaoli@dicp.ac.cn (G. Li).
[1] J.L. and H.A. contributed equally to this work.

http://dx.doi.org/10.1016/j.jcat.2015.07.020
0021-9517/

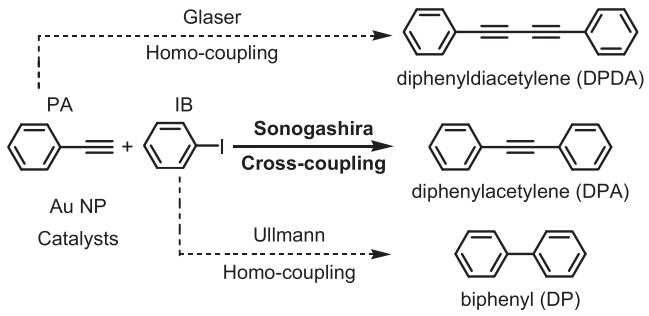

Scheme 1. Three possible reactions catalyzed on the surfaces of gold nanoparticles in the presence of phenylacetylene and iodobenzene, including Sonogashira cross-coupling (middle arrow) and two competitive homo-couplings (Glaser and Ullmann couplings, upper and lower arrows, respectively).

showed that the activation energy for bimolecular cross-coupling was comparable to that required for IB homo-coupling on Au(1 1 1) surfaces, which explained selectivity results obtained on catalysts that mainly contain neutral gold sites [19]. Experimental and theoretical studies have proposed that if positively charged Au sites (produced by either base or supports such as CeO_2) were present as well as neutral gold atoms, the activation energy of the Sonogashira cross-coupling reaction was minimized [19,20].

Shape-controlled metal nanoparticles possess well-defined surfaces and morphologies because their nucleation and growth are controlled at the atomic level [21,22]. Controlling the shape of nanoparticles can lead to increased functionality and selectivity in many catalytic reactions [23,24]. For example, Au nanorod catalysts often have aspect-ratio-dependent activity and generally perform much better in catalytic reactions than corresponding Au spherical nanoparticles [25]. Recently, well-defined gold nanorods were reported to exhibit better catalytic activity in hydrogenation of nitrobenzaldehyde into nitrobenzyl alcohol than Au spherical nanoparticle catalysts, which is mainly attributed to the drastic shape effect of the arrangement of surface Au atoms in the nanorod catalysts [26].

Physical and chemical properties of metal nanoparticles are distinctly influenced by their surface features and are subject to continuing interest from many research groups worldwide [27–29]. According to a recent spectroscopic experiment, Sonogashira cross-coupling is extremely sensitive to the details of catalysts' surface structure. It is shown that IB and PA react on well-developed crystalline Au(1 1 1) facets, but deliberately roughened gold surfaces are totally inert to the reactants [18,19]. Gold nanorods are prepared via a seed-mediated sequential growth process involving the use of 2−3 nm gold seed crystals and their subsequent growth in a series of reaction solutions containing $HAuCl_4$, $AgNO_3$, and cetyltrimethylammonium bromide (CTAB) [26,30,31]. The gold nanorods have an idealized 3-D prismatic morphology with 10 Au(1 1 1) end facets and 5 Au(1 0 0) side facets (Fig. S1 in the Supporting Information). These facets have different atomic arrangements on the surface, and thus intrinsically possess different electronic properties, surface free energy, adsorptions sites, and catalytic activity and selectivity for a given reaction. Therefore, it is both worthwhile and desirable to examine catalytic activity of gold nanorods when both (1 0 0) and (1 1 1) facets are present for reactions. There are no documented reports on catalytic performance of well-defined gold nanorods for carbon—carbon coupling reactions. To the best of our knowledge, no detailed experimental or calculated results are available in the literature to compare the Sonogashira cross-coupling on Au(1 1 1) and Au(1 0 0). With this objective, we focus here on the catalytic performance (including activity and selectivity) of well-defined gold nanorods for the Sonogashira cross-coupling reaction. The experimental studies have, in some cases, been complemented by DFT simulation to establish an understanding of structure–activity relationships and to pursue a fundamental mechanistic understanding of this catalytic process.

The outline of this study is as follows: First, we synthesize several gold colloids with different percentages of Au(1 1 1) and Au(1 0 0) facets, including gold nanoparticles (gold seeds and shapeless colloid I (Au/CTAB), where particle size is 2–4 and 20 nm, respectively) and gold nanorods with three different lengths (colloid II, 33 nm; colloid III, 42 nm; colloid IV, 50 nm). These colloids are protected by bilayer CTAB ligands. Next, we investigate the catalytic performance of the gold colloids in the Sonogashira cross-coupling reaction between *p*-iodoanisole and phenylacetylene. At the end, the mechanisms of homo- and cross-coupling reactions between IB and PA, i.e., IB adsorption and dissociation, surface diffusion of dissociated reactants, and surface coupling steps on Au(1 1 1) and Au(1 0 0) surfaces, are studied using DFT calculations. By combining experimental and DFT results, it is shown that the Au(1 1 1) surface functions better for the Sonogashira cross-coupling reaction and is more active and selective toward the desired cross-coupling product.

2. Experimental

2.1. Chemicals

$HAuCl_4{\cdot}3H_2O$ (99.99% metal basis, Aldrich), $AgNO_3$ (99% metal basis, Adamas), CTAB (98%, Adamas), sodium borohydride (99.99% metals basis, Aldrich), ascorbic acid (98%, Aldrich), *p*-iodoanisole (99%, Aldrich), phenylacetylene (99%, Aldrich), K_2CO_3 (99%, Adamas), *N,N*-dimethylformamide (DMF, 99%, Aldrich) were used as received. Nanopure water (resistance 18.2 MΩ cm) was purified with a Barnstead NANOpure Di-water TM system. All glassware was thoroughly cleaned with aqua regia ($HCl:HNO_3$ = 3:1 vol%), rinsed with copious Nano-pure water, and then dried in an oven prior to use.

2.2. Synthesis of gold seeds and gold colloids I–IV

According to reported protocols, gold seeds and gold colloids I–IV were synthesized through two main steps [26,30,31]. In the first step, CTAB (364 mg, 1 mmol) and $HAuCl_4{\cdot}3H_2O$ (1 mg, 0.0025 mmol) were dissolved in 10 mL nanopure water in a three-necked 25 mL round-bottom flask. $NaBH_4$ (0.6 mL, 10 mM) was added to the flask after 10 min, under vigorous magnetic stirring at room temperature for 30 min. The gold seeds were separated by centrifugation and stored in a freezer for the next step.

In the second step, CTAB (364 mg, 1 mmol), $HAuCl_4{\cdot}3H_2O$ (2 mg, 0.005 mmol), and $AgNO_3$(4 mM; 10 μL, 20 μL, 50 μL, and 100 μL for colloids I, II, III, and IV, respectively) were mixed with 10 mL nanopure water in a three-necked 25 mL round-bottom flask. Ascorbic acid (70 μL, 78.8 mM) was added to the flask after 10 min. Then Au seeds (12 μL) obtained from the first step were added to the mixture while the flask was immersed in a warm water bath at 27–30 °C. The reaction was stopped after 1 h and the excess CTAB was separated and removed by centrifugation (4000 rpm for 5 min). Further, these as-prepared Au colloids were characterized by UV–vis spectroscopy and transmission electron microscopy (TEM).

2.3. Characterization of gold nanoparticles

The UV–vis spectra of the Au nanoparticles (dissolved in water) were determined on a Hewlett-Packard (HP) Agilent 8453 diode

array spectrophotometer at room temperature. Powder X-ray diffraction (PXRD) data were collected on a DMAX2500 diffractometer using Cu Kα radiation. TEM images of the Au nanoparticles were obtained on a Hitachi 7000 transmission electron microscope operated at 75 kV. The specimen was made by placing one drop of a water solution of the Au nanoparticles on a carbon thin-film coated TEM grid. Fourier transform infrared (FT-IR) was performed on a Thermo/ATI/Mattson 60AR instrument (resolution, 1 cm^{-1}; scans, 16; range, 1000–4000 cm^{-1}).

2.4. Preparation of ~1 wt.% Au/CeO_2

According to previous works, CeO_2 can lead to higher catalytic efficiency in carbon—carbon coupling reactions (i.e., conversion and selectivity) of supported gold nanoclusters than other oxide supports (e.g., TiO_2, SiO_2, MgO) [15,16,32]. Free (unsupported) gold colloids are unstable at high temperatures (e.g., 100 °C), as the water solution turns colorless and formation of black solids at 100 °C is observed at the bottom of the flask for several hours (the black solids do not dissolve in the fresh water). Therefore, CeO_2 powder (100 mg) was added to a 5 mL solution of as-prepared Au colloids (initial concentration of gold: 0.5 mM in water, Fig. S2 in the Supporting Information). The mixtures were stirred for 12 h at room temperature and the supernatant became colorless. The ~1 wt.% Au/CeO_2 catalysts were collected by centrifugation and dried in vacuum. The Au/oxide catalysts were then heated at 200 °C in air for 2 h.

2.5. Procedure for the Sonogashira cross-coupling reaction

In a typical Sonogashira cross-coupling reaction, *p*-iodoanisole ($CH_3OC_6H_4I$, 0.1 mmol), phenylacetylene (0.12 mmol), K_2CO_3 (0.3 mmol), 1 wt.% Au/oxide (100 mg), and 1 mL DMF were added to a 5 mL one-necked round-bottom flask. Here we use *p*-iodoanisole and phenylacetylene as reactants only for ease of quantification by ^1H NMR [15]. The mixture was stirred under N_2 at 150 °C for 24 h as indicated in Table 1. After the catalytic reaction, 5 mL of water was added to the flask and the products were extracted twice by 2 mL of ethyl acetate and then characterized by ^1H NMR (300 MHz) after removal of ethyl acetate. Both the conversion of *p*-iodoanisole and selectivity for 4,4′-dimethoxy-1,1′-biphenyl and 1-methoxy-4-(2-phenylethynyl)benzene were determined by ^1H NMR spectroscopic analysis. As shown in Fig. S3 in the Supporting Information, the NMR analysis identified three components in the crude product, residual *p*-iodoanisole, which shows signals at δ = 3.79 ppm (—CH_3), the homo-coupling product 4,4′-dimethoxy-1,1′-biphenyl (DMBP) at 3.85 ppm (—CH_3), and the cross-coupling product 1-methoxy-4-(2-phenylethynyl) benzene (MPEB) at 3.87 ppm (—CH_3).

2.6. Computational details

Periodic DFT calculations were performed to investigate mechanisms of the Sonogashira cross-coupling reaction between IB and PA and the competitive Ullmann homo-coupling reaction on two types of gold surfaces: Au(111) and Au(100). The Projector Augmented-Wave (PAW) method was used to describe the interaction between the electrons and nuclei [33]. The Perdew–Burke–Ernzerhof (PBE) form of the generalized gradient approximation was employed for electron exchange and correlation [34,35]. The kinetic energy cutoff was chosen to be 450 eV and integration in the reciprocal space was carried out at the Γ *k*-point of the Brillouin zone. The reaction energy for a given process is defined as

$$\Delta E = \sum E_{pro} - \sum E_{rea},$$

where $\sum E_{pro}$ and $\sum E_{rea}$ are the total energies of the products and reactants, respectively. The nudged elastic band (NEB) approach and frequency analysis were used for identifying transition states [36]. The theory of atoms in molecules proposed by Bader was applied to estimate partial charges [37–39].

The Au(100) and Au(111) extended surfaces were modeled, respectively, by (6 × 6) and (5 × 5) supercell slabs containing 36 and 50 atoms in two layers. The size of unit cells used for the computations are 12.50 × 12.50 × 40.00 Å and 14.60 × 14.60 × 40.00 Å for Au(100) and Au(111) models, respectively. These models are large enough to accommodate the adsorbed species (e.g., IB) while avoiding lateral interactions. The top layers of the gold slabs and the adsorbates were allowed to relax fully during the geometry optimizations. The gold atoms in the lower layer were kept fixed at their optimized bulk positions. All calculations were carried out with the Quantum Espresso package [40].

3. Results and discussion

3.1. Characterization of the Au nanoparticles

The Au nanorods were synthesized via a two-step method [30,31]. First, gold seeds were prepared via reduction of $HAuCl_4$ by $NaBH_4$ in the presence of excess CTAB. Next, the gold seeds grew in the Au(III)/CTAB solution with different amounts of Ag(I) salt. Finally, the gold nanoparticles Au/CTAB (colloid I) and gold nanorods (colloids II, III, and IV) with different sizes were obtained (see details in the *Experimental* section).

The as-prepared gold seeds and colloids I–IV are characterized by UV–vis spectroscopy and TEM, as shown in Fig. 1. In the case of gold seeds, a shoulder peak can be seen around 520 nm, which corresponds to the red color[2] of the gold seed solution (Fig. 1F, dotted line). As illustrated in Fig. 1A, the TEM image indicates that the size of the gold seeds is 2–4 nm. The water solution of gold colloid I also appears in red and the shoulder in the UV–vis spectrum becomes an obvious absorption peak around 530 nm (Fig. 1F, black line). The TEM image suggests that the size of the gold colloid I is 20 ± 4 nm (Fig. 1B). The gold seeds and colloid I are shapeless, as evidenced by TEM analysis. The gold colloids II, III, and IV turn out to be violet, deep blue, and pink in water, respectively. As shown in Fig. 1F, the later gold colloids show two absorption peaks in the UV–vis spectrum (~535 and 600 nm for colloid II, ~560 and 670 nm for colloid III, and ~530 and 750 nm for colloid IV). According to TEM images, lengths of Au colloids are 33 ± 5 (width: 21 ± 3 nm), 42 ± 3 (width: 15 ± 2 nm), and 50 ± 4 nm (width: 13 ± 1 nm) for gold colloids II, III, and IV, respectively (Fig. 1C–E). The aspect ratio of length to width for the gold colloids is ca. 1.6 (colloid II), 2.8 (colloid III), and 3.9 (colloid IV). The optical properties of the Au colloids are consistent with the TEM analysis. Unlike the gold seeds and colloid I, the gold colloids (II, III, and IV) possess a nanorod-like shape.

3.2. Catalytic performance of the Au colloids in Sonogashira cross-coupling reactions

The results for the catalytic efficiency of gold seeds and colloids I–IV in carbon—carbon coupling reactions are compiled in Table 1. We first note that Au seed catalyst yields 25% conversion of *p*-iodoanisole to 4,4′-dimethoxy-1,1′-biphenyl (DMBP) and 1-methoxy-4-(2-phenylethynyl) benzene (MPEB) with 37% selectivity for MPEB (Table 1, entry 1). Hereafter, the conversion is based on consumption of *p*-iodoanisole, as the phenylacetylene is excess. Also, the selectivity is calculated with respect to production

[2] For interpretation of color in Fig. 1, the reader is referred to the web version of this article.

Table 1
The catalytic activity and selectivity of the gold nanoparticles supported on ceria in Sonogashira cross-coupling reactions between *p*-iodoanisole and phenylacetylene[a]:

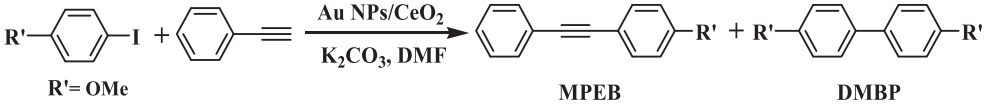

Entry	Catalyst	Conv. (%)[b]	Selectivity (%)[b]	
			MPEB	DMBP
1	Au seeds	25	37	63
2	Colloid I	16	59	41
3	Colloid II	57	90	10
4	Colloid III	36	54	46
5	Colloid IV	34	48	52
6	CTAB + CeO_2	n.r.		

[a] Reaction conditions: 100 mg Au/CeO_2 catalyst (1 wt.% Au nanoparticles loading), 0.1 mmol *p*-iodoanisole, 0.12 mmol phenylacetylene, 0.3 mmol K_2CO_3, 1 mL DMF, 150 °C, 24 h.
[b] The conversion of 4-iodoanisole and selectivity for DMBP and MPEB were determined by ^{1}H NMR. Conv. = conversion, n.r. = no reaction.

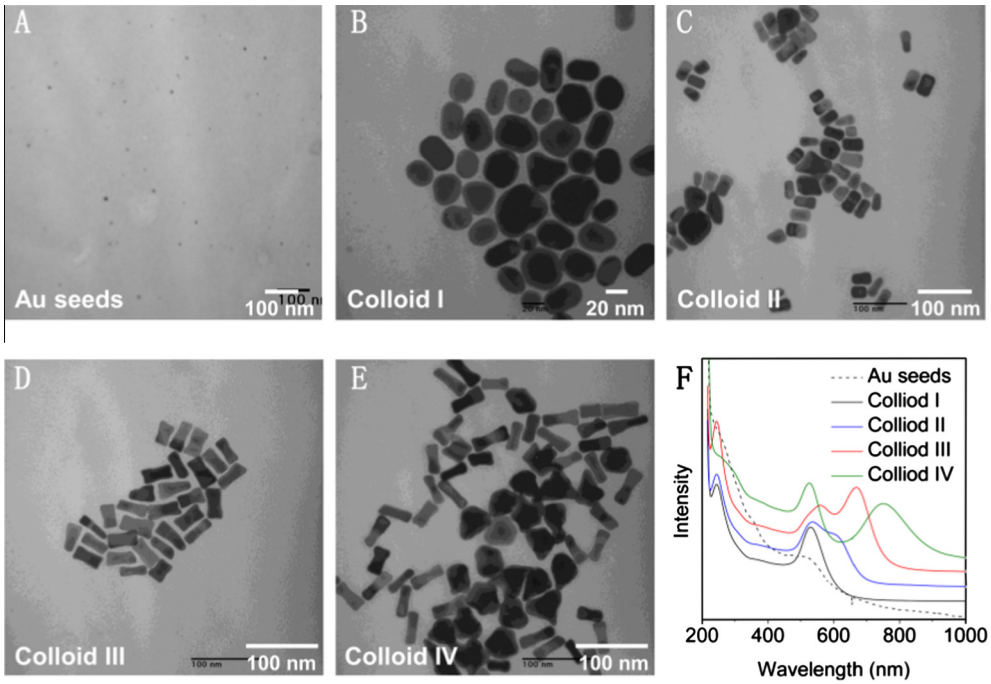

Fig. 1. (A–E) TEM images and (F) UV–vis spectra of the gold seeds and the gold colloids I–IV. Scale bars in A, C, D, and E are 100 nm, and 20 nm in B.

of MPEB, which is the desired cross-coupling product. The gold nanoparticles Au/CTAB (colloid I) show minimal conversion (16%) among all the gold nanoparticles, with 59% selectivity (Table 1, entry 2). Interestingly, the conversion and selectivity improve markedly to 57% and 90%, respectively, when colloid II is used as the catalyst (Table 1, entry 3). The gold colloids III and IV result in moderate increases in catalytic efficiency (Table 1, entries 4 and 5). Our results indicate that well-defined nanorods (colloid II, III, and IV) generally show better catalytic efficiency and selectivity than shapeless nanoparticles (colloid I), and the gold colloid II catalyst exhibits the best catalytic performance among the five catalysts.

3.3. Mechanism of the coupling reactions

High-resolution TEM in previous studies indicates that the Au nanorods adopt a penta-twinned structure [41–44]. The two ends of the nanorods form a decahedron fully enclosed by ten Au(111) facets, while the sides are terminated by Au(100). Therefore, coupling reactions on the gold nanorods raise an interesting question: how do Au(111) and Au(100) facets contribute to homo- and cross-coupling reactions? To get a qualitative understanding of facet effects on the coupling reactions, we investigate IB adsorption and dissociation and surface homo- and cross-coupling steps using DFT simulation.

3.3.1. IB adsorption and dissociation

Our studies show that IB adsorbs on Au(100) and Au(111) with Au—I distance 2.95 and 2.86 Å, respectively ($Re_1 \rightarrow Im1_1$, Fig. 2). We note that the C—I bond is more elongated on Au(111) than on Au(100). For comparison, the equilibrium C—I bond length of an isolated IB is 2.09 Å. Next, C—I bond dissociation takes place through a transition state ($Im_1 \rightarrow Im2_1$), and the phenyl group is placed on top of an Au atom ($Im2_1 \rightarrow Pr_1$). Also, the iodine atom becomes strongly chemisorbed on bridging and hollow sites of the Au(100) and Au (111) models, respectively. Calculated

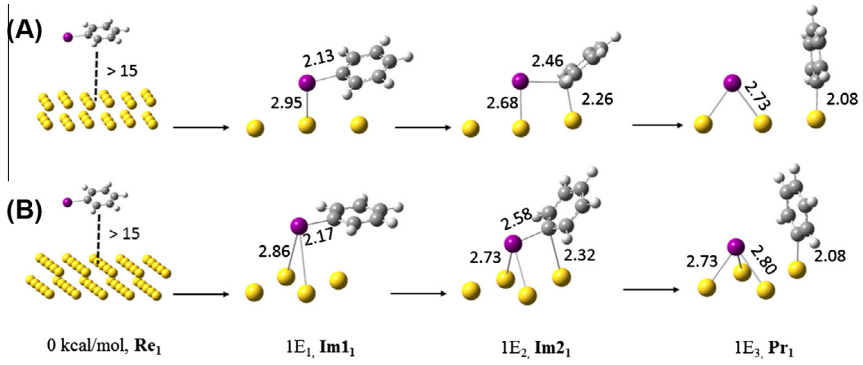

Fig. 2. Proposed Mechanism 1 for C—I bond dissociation of IB on extended (A) Au(100) and (B) Au(111) surfaces. The values of interatomic distances are measured in units of Å. The calculated energies for different steps relative to the reactant state Re_1 (isolated IB and Au slabs) are given in Table 2. Color code: Au, yellow; C, gray; H, white; and I, purple. For clarity, not all the gold atoms of slabs for steps $Im1_1$, $Im1_2$, and Pr_1 are shown. (For interpretation of the references to color in this figure legend, the reader is referred to the web version of this article.)

Table 2
DFT results for adsorption, activation, and reaction energies (kcal/mol) of the elementary steps of the coupling reactions over Au(100) and Au(111).

	Au(100)	Au(111)[a]
Re_1, Re_2, and Re_3	0	0
E_{ads} IB = $1E_1$	−7.0	−10.6 (−7.0)
E_{act} IB = $1E_2 - 1E_1$	20.3	16.1 (15.7)
$1E_3$	−23.0	−20.5
$2E_1$	4.4	7.9
$2E_2$	9.0	2.5
E_{act} BP = $2E_3 - 2E_2$	29.5	27.5 (31.8)
$2E_4$	−26.7	−33.6
E_{act} DPA = $3E_1$	37.8	28.1 (30.0)
$3E_2$	−19.8	−14.0

Note: The calculated energies are relative to the reactant states Re_1, Re_2, and Re_3.
[a] Results reported in Ref. [19] are given in parentheses to compare with those obtained in our study.

adsorption and activation energies are compiled in Table 2. In good agreement with previous studies [19,45], the adsorption process is found to be exothermic by 7.0 and 10.6 kcal/mol on Au(100) and Au(111), respectively. Though dispersion corrections are not included in our calculations, we believe that such corrections stabilize IB adsorption on the Au(111) surface better than on Au(100), mainly because the planar density of Au(111) is basically greater than that of Au(100) (more atoms per area; see the *Experimental* section). It is worthwhile to note that the activation energy (E_{act} IB = $1E_2 - 1E_1$) for IB dissociation on the Au(111) surface is 4.2 kcal/mol less than that on Au(100). Thus, the results calculated above indicate that the Au(111) facet may provide a much better platform for IB adsorption and C—I bond dissociation in gold-catalyzed coupling reactions.

The surface reactivity is correlated with the electronic structure. With these concepts in mind, the projected density of states (PDOS) is analyzed for the valence electrons of Re_1 and $Im1_1$ (Fig. 2). The PDOS analyses are useful for understanding the details of the interaction between the Au(111) and Au(100) facets and IB. The PDOS is calculated by projecting the electron wave functions onto spherical harmonics centered on each type of metal atom. Figs. S4A and S4B, in the Supporting Information, show plots of the PDOS of the *d*-, *p*-, and *s*-states of the models before adsorption of IB (Re_1). Distance between the gold surface and IB is greater than 15 Å, which refers to a noninteracting state of the systems. The zero energy of the plots is set at the Fermi energy of Re_1 in the Au(100) model as reference. Two aspects are noteworthy. First, the states of the Au(100) surface are located at lower energy levels than those of the Au(111) surface. Second, the states of noninteracting IB, specifically *p*(I), overlap better with the *d*-states of Au(111) than those of Au(100). This indicates that, from the electronic point of view, the Au(111) surface is probably more accessible for the adsorbates to react with.

Figs. S4C and S4D, in the Supporting Information, show plots of the PDOS of the *d*-, *p*-, and *s*-states of the models after adsorption of IB ($Im1_1$), indicating that such states are broadened and delocalized compared with the noninteracting systems (Re_1). It is worthwhile to note that broadening and delocalization of states are more pronounced for the Au(111) surface than for the Au(100) surface. In turn, this can show stronger hybridization between Au(111) states and IB states, indicating stronger bond formation between Au and I atoms. Further, we conduct Bader charge analyses to understand charge transfer between Au models and IB after adsorption [37–39]. Partial charges of different fragments for elementary steps in Fig. 2 are compiled in Table S1 in the Supporting Information. Though the partial charge of the phenyl group remains the same (∼−0.76*e*, where *e* = elementary charge) as before adsorption of IB, the iodine atom and gold slabs are engaging in strong charge transfer during the adsorption process. Our calculations show that the partial charges of iodine and Au(100) model are +1.01*e* and −0.24*e*, respectively. In the case of the Au(111) model, they are found to be +1.15*e* and −0.41*e*. This indicates that charge transfer between iodine and gold atoms is stronger in the Au(111) model than in the Au(100) model, which is in line with the results of the PDOS analysis and Au—I bond distances (Fig. 2). These aspects explain why the adsorption energy of IB on Au(111) is greater than that on Au(100).

Upon IB dissociation on surfaces, iodine atoms strongly adsorb on the gold atoms. Therefore, the possibility of catalyst poisoning by iodine atoms is considered. The interaction energies, E_1^{int} and E_2^{int}, between iodine atoms and gold slabs were calculated according to

$$E_1^{int} = E(\text{I—Au slab}) - E(\text{Au slab}) - 1/2E(I_2)$$

$$E_2^{int} = E(\text{I—Au slab}^-) - E(\text{Au slab}) - E(I^-),$$

where E(I—Au slab) and E(I—Au slab$^-$) are the total energy of iodine atoms adsorbed on the neutral and negatively charged catalyst models. E(Au slab) is the total energy of the catalyst models. $E(I_2)$ and $E(I^-)$ are the total energy of I_2 molecules and anion I^- in the gas phase. Our calculations show that $E^{int}_{1,Au(111)} - E^{int}_{1,Au(100)}$ and $E^{int}_{2,Au(111)} - E^{int}_{2,Au(100)}$ are 0.1 and 7.0 kcal/mol, indicating that both of the Au(100) and Au(111) facets can be poisoned by iodine atoms.

3.3.2. Surface coupling

Surface diffusion of reactants on heterogeneous catalysts is a critically important concept [46,47]. Reaction rates are often

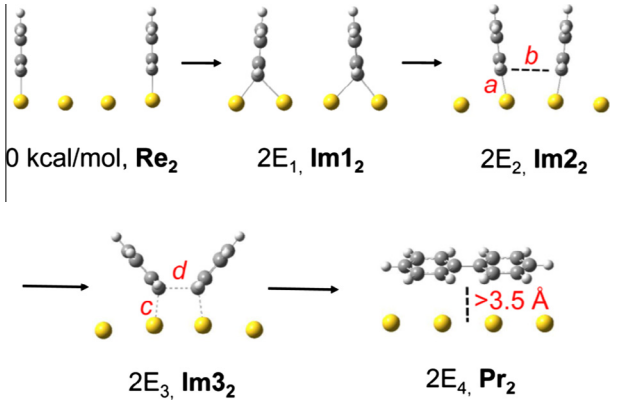

Fig. 3. Proposed Mechanism 2 for homo-coupling reaction through a stepwise approach. The values of interatomic distances for Au(100) and Au(111) surfaces are a = 2.08 and 2.07, b = 3.90 and 3.69, c = 2.22 and 2.19, and d = 2.30 and 2.27 Å, respectively. See Table 2 for the calculated energies of different steps relative to Re_2. Color code: Au, yellow; C, gray; H, white. (For interpretation of the references to color in this figure legend, the reader is referred to the web version of this article.)

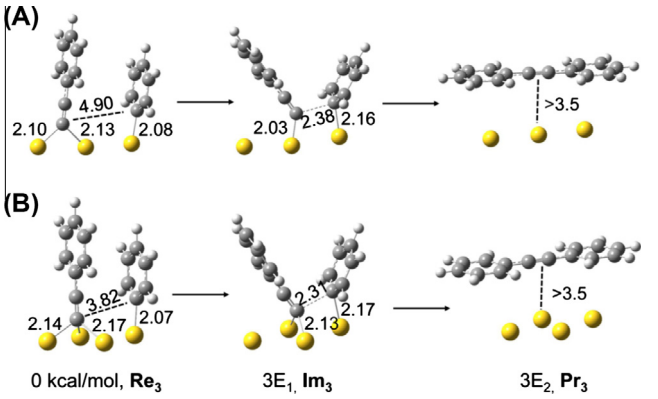

Fig. 4. Proposed Mechanism 3 for cross-coupling reaction on extended (A) Au(100) and (B) Au(111) surfaces. See Table 2 for the calculated energies for different steps relative to the reactants state Re_3. Unit for distance: Å. Color code: Au, yellow; C, gray; H, white. (For interpretation of the references to color in this figure legend, the reader is referred to the web version of this article.)

affected by the ability of reactants to find each other at a catalyst surface. Fig. 3 shows a possible mechanism (Mechanism 2) for two phenyl groups to move toward each other and form a new C—C bond (homo-coupling) on Au(100) and Au(111) surfaces. Calculated energies of different steps (Table 2) indicate that $Re_2 \rightarrow Im1_2 \rightarrow Im2_2 \rightarrow Im3_2$ is a continuous endothermic process on the Au(100) surface. Interestingly, $Im1_2 \rightarrow Im2_2$ is an exothermic process on the Au(111) surface, though $Re_2 \rightarrow Im1_2$ and $Im2_2 \rightarrow Im3_2$ steps are endothermic. We think that stabilization of $Im2_2$ is mainly due to the π–π stacking interaction of two neighboring phenyl groups that are located closer to each other on Au(111) than on Au(100) (see the interatomic distance b, Fig. 2). As Table 2 shows, the rate-determining step of biphenyl (BP) formation is the bimolecular surface coupling reaction. We particularly note that the activation energies (E_{act} BP) for the homo-coupling reaction on Au(100) and Au(111) are comparable. The homo-coupling product (BP) can adsorb onto the catalysts' surfaces (Pr_2). The Bader charge analyses (Table S1 in the Supporting Information) show that charge transfer from π electrons of phenyl rings to Au(111) is stronger than that to Au(100). This suggests that BP interacts more favorably with Au(111) surface than with Au(100).

Fig. 4 shows a proposed mechanism (Mechanism 3) for the cross-coupling reaction producing DPA on Au(100) and Au(111) models, where phenylacetylene and iodobenzene are used in the DFT calculation. There are several noteworthy aspects. In the case of Re_3, a phenyl group is placed on top of a gold atom for both models, but the phenylacetylenyl fragment (Ph—C≡C—) is adsorbed on bridging and threefold hollow sites of Au(100) and Au(111) facets, respectively. The coordination number of the C atom of Ph—C≡C— involved in the cross-coupling reaction is 3 and 4 on Au(100) and Au(111) facets, respectively (Re_3, Fig. 4). Interatomic distances of carbon atoms of the phenyl and phenylacetylenyl fragments that form new C—C bonds are considerably larger on the Au(100) surface (4.90 and 2.38 Å versus 3.82 and 2.31 Å, Re_3 and Im_3). Table 2 shows, as in the homo-coupling case, the rate-determining step of DPA formation is the bimolecular surface coupling reaction. It is worth mentioning that the activation energy of the cross-coupling reaction (28.1 kcal/mol, $Re_3 \rightarrow Im_3$) is comparable to that required for homo-coupling (27.5 kcal/mol) of phenyl groups on Au(111) surface, in good agreement with a previous study [19]. For the case of Au(100), the activation energy of the cross-coupling reaction is 8.3 kcal/mol higher than that for the homo-coupling reaction. These calculated results clearly suggest that the Au(100) surface may prefer to yield a homo-coupling product (BP). Upon formation of the cross-coupling product, DPA adsorbs onto the surface gold atoms (Pr_3). The Bader charge analyses for step Pr_3 show that charge transfer occurs from Au(100) to DPA (Table S1 in the Supporting Information). This means that the surface gold atoms are positively charged. For the case of Au(111), charge transfer is interestingly in a reversed manner: the surface gold atoms are negatively charged. Comparison of partial charges of the gold slabs (Table S1 in the Supporting Information) for different steps presented in Figs. 2–4 suggests that Au(111) and Au(100) may possess better electron withdrawing and donating characteristics, respectively.

To investigate surface diffusion of Ph—C≡C— on the catalyst models, we consider two possible pathways that the fragment may follow to approach a phenyl group in the cross-coupling reaction (Fig. 5). For both pathways, a phenyl group is placed on top of a gold atom. Our calculations show that the adsorption energy of Ph—C≡C— on bridging sites of the Au(100) surface is 10.6 kcal/mol higher than that on the top site (Fig. 5A). It is also found that adsorption on the fourfold hollow site is 5.2 kcal/mol less favored than on the top site. This result indicates that Ph—C≡C— may diffuse on the Au(100) surface, which tends toward a mechanism that involves migration through bridging site → on-top site → bridging site. As Fig. 5B shows, threefold hollow and bridging are the most preferred adsorption sites for Ph—C≡C— on the Au(111) surface. Also, there is a big difference in the energetics of adsorption on the mentioned (threefold hollow and bridging) and on top sites (~14.0 kcal/mol). This strongly indicates that surface diffusion of Ph—C≡C— on the Au(111) surface toward a phenyl group in the cross-coupling reaction takes place mainly through the pathway threefold hollow site → bridging site → threefold hollow site (Fig. 5B). It is also worthwhile to compare Ph—C≡C— adsorption energetics on different sites of Au(100) and Au(111) surfaces. We particularly note that the energy difference of two preferred adsorption sites is considerably lower for Au(111) than for Au(100). The difference in energy for Au(111) is 5.7 kcal/mol (threefold hollow versus bridging), while it is 10.6 kcal/mol for Au(100) (bridging versus on-top). These results lead us to conclude that surface diffusion of Ph—C≡C— is markedly higher on Au(111) than on Au(100).

We pause here for perspective. While the exact mechanism of the growth of the nanoparticles is not yet fully resolved, it is believed to operate as a zipper mechanism [46]. In this mechanism, the gold nanorods grows while the surfactant (CTAB) immediately assembles along the crystalline Au(100) facet, preventing growth

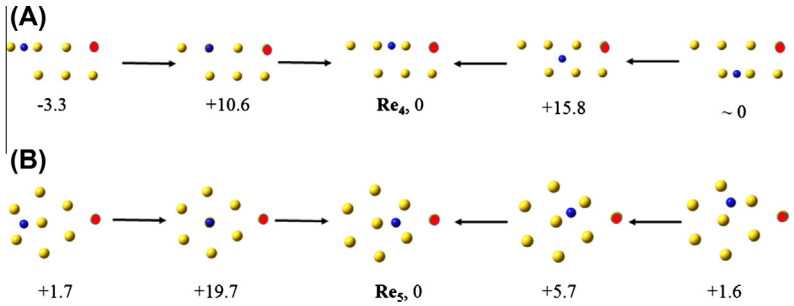

Fig. 5. Two possible pathways for surface diffusion of the phenylacetylenyl fragment (Ph—C≡C—) to approach a phenyl (Ph—) group in a cross-coupling reaction on (A) Au(100) and (B) Au(111). The calculated energies for different steps relative to Re_4 and Re_5 are given in kcal/mol for each model. The phenylacetylenyl fragment and the phenyl group are shown by a blue and a gray ball, respectively, for simplicity. Color code: Au, yellow; phenyl group, red; phenylacetylenyl fragment, blue. For clarity, other gold atoms of slabs are not shown. (For interpretation of the references to color in this figure legend, the reader is referred to the web version of this article.)

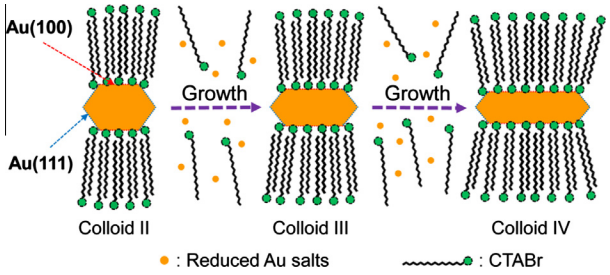

Scheme 2. Proposed zipper mechanism of the gold nanorods [48]. The CTAB surfactant hinders the growth of specific crystalline facets, resulting in anisotropic growth and the formation of gold nanorods.

in that direction (nanorod sides). With the aid of Ag^+ ions, isotropical growth of the particle is directed along the (001) axis with Au(111) facets (Scheme 2) [49,50]. As the length of the gold nanorods increases, the percentage of the gold atoms with the Au(111) facet decreases, which is supported by the powder XRD analysis (Fig. 6). XRD analysis indicates that the intensity ratio of Au(200) (diffraction angle 2θ at 44.8°) to Au(111) ($2\theta = 38.4°$) is higher for colloid IV than for colloid II. The Au(100) facet of the Au nanorods has a higher surface energy and the side facets of nanorods interact well with the surfactant (CTAB) [42–44]. In other words, the decahedron of Au nanorods with the Au(111) surface is less covered by CTAB surfactants and is probably the most accessible part of the gold particles for the reactions. However, due to the high temperature of the reaction media, removal of surfactant CTAB is expected. To verify this assumption, we measured the FT-IR spectra of two samples of colloid II: (1) fresh colloid II sample, as explained in the *Experimental* section, and (2) colloid II sample treated in DMF at 150 °C (i.e., the reaction conditions) for 2 h, collected by centrifugation, and washed with ethanol three times prior to FT-IR measurement. The results clearly show that colloid II loses many CTAB under the reaction conditions, evidenced by the obvious decrement of peak intensities at 2960, 2925, and 2854 cm^{-1} (Fig. S5 in the Supporting Information).

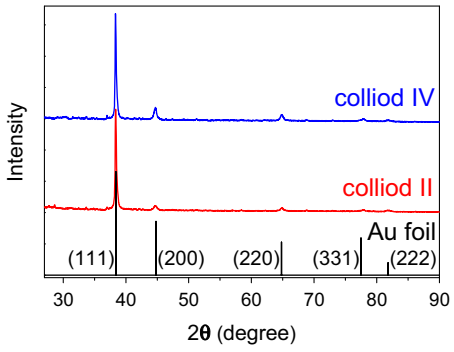

Fig. 6. Powder XRD of the samples of colloids II and IV. The black stick pattern corresponds to the bulk gold fcc structure (gold foil). The diffraction angle at 38.4° is assigned to Au(hkl = 111), 44.8° to Au(200), 64.8° to Au(220), 77.5° to Au(311), and 81.8° to Au(222).

Nanorod sides have some degree of crystalline Au(110) facet [41–44], which has the higher surface energy, and is assumed to be stabilized by the surfactant molecules (e.g., CTAB) [51]. The Au(220) facet is observed in the powder XRD analysis of both colloids II and VI (Fig. 6). Since the Au(110) facet is believed either not to be stable or only to exist at the edges of nanorods sides, implying a very low percentage of this facet [48], we exclude the DFT calculations on the Au(110) facet. Calculations of transition states show that the homo-coupling reaction is feasible on both surfaces, but the cross-coupling reaction is more probable on Au(111). DFT calculations suggest that interaction of iodine atoms with Au(100) might be stronger, and the corresponding catalyst poisoning by iodine atoms may be more important. Also, dissociated reactants on the surfaces of catalysts, especially for cross-coupling reactions, are found to be more diffusive on Au(111) than on Au(100).

It is well known that the electric field on the metal surface is perpendicular to the surface, and its strength is proportional to the surface charge density. The charge density is higher at the sharp edges of metals. Therefore, it is expected that molecules will have a stronger interaction with the sharp edges of the nanoparticles' surface. For example, it is shown that IB dissociation is more feasible on low-coordinated Au atoms at corner sites [19]. Previous DFT and experimental results have shown the positive role played by cationic gold in the Sonogashira cross-coupling reaction. The presence of both neutral and cationic gold on the catalyst surface reduces the activation energy of the rate-determining step of cross-coupling reactions [19]. All of these facts lead us to expect better conversion and selectivity toward the cross-coupling reaction on decahedra of Au nanorods where a considerable percentage of gold atoms are located at the corners. Thus, the catalytic activity (including the conversion of 4-iodoanisole and the selectivity for the cross-coupling product) of the gold nanorods should decrease as the length of the nanorods is increased. This means that longer gold nanorod catalysts are preferred to yield homo-coupling product instead of cross-coupling product.

4. Conclusions

We investigated the catalytic activity of bilayer CTAB-protected gold nanoparticles and surface well-defined nanorods for the Sonogashira cross-coupling reaction between phenacetylene and *p*-iodoanisole. It is found that gold nanorods (colloids II, III, IV)

exhibit better catalytic performance than the corresponding gold nanoparticles (Au seeds and colloid I, which are surface undefined). Among all the nanorods, the shorter ones with a higher percentage of Au(111) faceting show better catalytic performance with moderate conversion (57%) and high selectivity toward the cross-coupling product (90% selectivity for 1-methoxy-4-(2-phenylethynyl) benzene). Using DFT calculations, we examine the roles played by Au(100) and Au(111) surfaces of the gold nanorods. It is found that coupling reactions are more favorable to occur on Au(111) than on Au(100).

Acknowledgments

G.L. acknowledges financial support by the startup funds of the Dalian Institute of Chemical Physics and the "Thousand Youth Talents Plan".

Appendix A. Supplementary material

Supplementary data associated with this article can be found, in the online version, at http://dx.doi.org/10.1016/j.jcat.2015.07.020.

References

[1] R. Chinchilla, C. Najera, Chem. Soc. Rev. 40 (2011) 5084.
[2] L. Yin, J. Liebscher, Chem. Rev. 107 (2007) 133.
[3] O. Daugulis, H. Do, D. Shabashov, Acc. Chem. Res. 42 (2009) 1074.
[4] F. Monnier, M. Taillefer, Angew. Chem., Int. Ed. 48 (2009) 6954.
[5] R. Martin, S.L. Buchwald, Acc. Chem. Res. 41 (2008) 1461.
[6] G. Kyriakou, S.K. Beaumont, S.M. Humphrey, C. Antonetti, R.M. Lambert, ChemCatChem 2 (2010) 1444.
[7] M. Lamblin, L. Nassar-Hardy, J.C. Hierso, E. Fouquet, F.X. Felpin, Adv. Synth. Catal. 352 (2010) 33.
[8] M. Stratakis, H. Garcia, Chem. Rev. 112 (2012) 4469.
[9] G. Li, R. Jin, Nanotechnol. Rev. 5 (2013) 529.
[10] A. Corma, H. Garcia, Chem. Soc. Rev. 37 (2008) 2096.
[11] M. Haruta, Cattech 6 (2002) 102.
[12] A. Taketoshi, M. Haruta, Chem. Lett. 43 (2014) 380.
[13] G. Li, R. Jin, Acc. Chem. Res. 46 (2013) 1749.
[14] S. Yamazoe, K. Koyasu, T. Tsukuda, Acc. Chem. Res. 47 (2014) 816.
[15] G. Li, D. Jiang, C. Liu, C. Yu, R. Jin, J. Catal. 306 (2013) 177.
[16] G. Li, C. Liu, Y. Lei, R. Jin, Chem. Commun. 48 (2012) 12005.
[17] S.K. Beaumont, G. Kyriakou, R.M. Lambert, J. Am. Chem. Soc. 132 (2010) 12246.
[18] V.K. Kanuru, G. Kyriakou, S.K. Beaumont, A.C. Papageorgiou, D.J. Watson, R.M. Lambert, J. Am. Chem. Soc. 132 (2010) 8081.
[19] M. Boronat, D. Combita, P. Concepción, A. Corma, H. García, R. Juárez, S. Laursen, J.D. López-Castro, J. Phys. Chem. C 116 (2012) 24855.
[20] C. González-Arellano, A. Abad, A. Corma, H. García, M. Iglesias, F. Sánchez, Angew. Chem., Int. Ed. 46 (2007) 1536.
[21] C.J. Murphy, T.K. San, A.M. Gole, C.J. Orendorff, J.X. Gao, L. Gou, S.E. Hunyadi, T. Li, J. Phys. Chem. B 109 (2005) 13857.
[22] C.J. Murphy, A.M. Gole, S.E. Hunyadi, J.W. Stone, P.N. Sisco, A. Alkilany, B.E. Kinard, P. Hankins, Chem. Commun. 5 (2008) 544.
[23] K.M. Bratlie, H. Lee, K. Komvopoulos, P. Yang, G.A. Somorjai, Nano Lett. 7 (2007) 3097.
[24] R. Narayanan, M.A. El-Sayed, J. Phys. Chem. B 109 (2005) 12663.
[25] A.R. Tao, S. Habas, P.D. Yang, Small 4 (2008) 310.
[26] G. Li, C. Zeng, R. Jin, J. Phys. Chem. C 119 (2015) 11143.
[27] A. Fihri, M. Bouhrara, B. Nekoueishahraki, J.M. Basset, V. Polshettiwar, Chem. Soc. Rev. 40 (2011) 5181.
[28] J.K. Bording, B.Q. Li, Y.F. Shi, J.M. Zuo, Phys. Rev. Lett. 90 (2003) 226104.
[29] C. Burda, X.B. Chen, R. Narayanan, M.A. El-Sayed, Chem. Rev. 105 (2005) 1025.
[30] N.R. Jana, L. Gearheart, C.J. Murphy, J. Phys. Chem. B 105 (2001) 4065.
[31] B. Nikoobakht, M.A. El-Sayed, Chem. Mater. 15 (2003) 1957.
[32] R.O.M.A. de Souza, M.S. Bittar, L.V.P. Mendes, C.M.F. da Silva, V.T. da Silva, O.A.C. Antunes, Synlett (2008) 1777.
[33] P.E. Blöchl, Phys. Rev. B 50 (1994) 17953.
[34] J.P. Perdew, K. Burke, M. Ernzerhof, Phys. Rev. Lett. 77 (1996) 3865.
[35] J.P. Perdew, K. Burke, M. Ernzerhof, Phys. Rev. Lett. 78 (1997) 1396.
[36] G. Henkelman, B.P. Uberuaga, H. Jonsson, J. Chem. Phys. 113 (2000) 9901.
[37] W. Tang, E. Sanville, G. Henkelman, J. Phys.: Condens. Matter 21 (2009) 084204.
[38] E. Sanville, S.D. Kenny, R. Smith, G. Henkelman, J. Comput. Chem. 28 (2007) 899.
[39] G. Henkelman, A. Arnaldsson, H. Jónsson, Comput. Mater. Sci. 36 (2006) 254.
[40] P. Giannozzi, S. Baroni, N. Bonini, M. Calandra, R. Car, C. Cavazzoni, D. Ceresoli, G.L. Chiarotti, M. Cococcioni, I. Dabo, A. Dal Corso, S. Fabris, G. Fratesi, S. de Gironcoli, R. Gebauer, U. Gerstmann, C. Gougoussis, A. Kokalj, M. Lazzeri, L. Martin-Samos, N. Marzari, F. Mauri, R. Mazzarello, S. Paolini, A. Pasquarello, L. Paulatto, C. Sbraccia, S. Scandolo, G. Sclauzero, A.P. Seitsonen, A. Smogunov, P. Umari, R.M. Wentzcovitch, J. Phys.: Condens. Matter 21 (2009) 395502.
[41] M.Z. Liu, P. Guyot-Sionnest, J. Phys. Chem. B 109 (2005) 22192.
[42] A.S. Barnard, L.A. Curtiss, J. Mater. Chem. 17 (2007) 3315.
[43] X. Bai, Y. Gao, H. Liu, L. Zheng, J. Phys. Chem. C 113 (2009) 17730.
[44] N. Garg, C. Scholl, A. Mohanty, R. Jin, Langmuir 26 (2010) 10271.
[45] C. Sánchez-Sánchez, F. Yubero, A.R. González-Elipe, L. Feria, J.F. Sanz, R.M. Lambert, J. Phys. Chem. C 118 (2014) 11677.
[46] Y.N. Mo, W.G. Zhu, E. Kaxiras, Z.Y. Zhang, Phys. Rev. Lett. 101 (2008) 216101.
[47] T.G. Mattos, F.D.A. Aarão Reis, J. Catal. 263 (2009) 67.
[48] J.X. Gao, C.M. Bender, C.J. Murphy, Langmuir 19 (2003) 9065.
[49] B. Nikoobakht, M.A. El-Sayed, Langmuir 17 (2001) 6368.
[50] M.J. Walsh, S.J. Barrow, W. Tong, A.M. Funston, J. Etheridge, ACS Nano 9 (2015) 715.
[51] P.L. Gai, M.A. Harmer, Nano Lett. 2 (2002) 771.